The Journal of Chemical Physics

RESEARCH ARTICLE | JULY 02 2024

Interplay of chemotactic force, Péclet number, and dimensionality dictates the dynamics of auto-chemotactic chiral active droplets

Special Collection: 2024 JCP Emerging Investigators Special Collection

Chung Wing Chan ; Zheng Yang ; Zecheng Gan ; Rui Zhang

Check for updates

J. Chem. Phys. 161, 014904 (2024)
https://doi.org/10.1063/5.0207355

View Online
Export Citation

Articles You May Be Interested In

Computational kinetic study of chemotactic cell migration

J. Appl. Phys. (October 2013)

Chemotactic behavior of spermatozoa captured using a microfluidic chip

Biomicrofluidics (March 2018)

The stability of a homogeneous suspension of chemotactic bacteria

Physics of Fluids (April 2011)

22 January 2025 20:28:18

AIP Publishing

AIP Publishing
The Journal of Chemical Physics
Special Topics Open for Submissions
Learn More

The Journal of Chemical Physics ARTICLE pubs.aip.org/aip/jcp

Interplay of chemotactic force, Péclet number, and dimensionality dictates the dynamics of auto-chemotactic chiral active droplets

Cite as: J. Chem. Phys. 161, 014904 (2024); doi: 10.1063/5.0207355
Submitted: 7 March 2024 • Accepted: 31 May 2024 •
Published Online: 2 July 2024

View Online Export Citation CrossMark

Chung Wing Chan,[1,2,a)] Zheng Yang,[2,3] Zecheng Gan,[2,4,b)] and Rui Zhang[1,c)]

AFFILIATIONS

[1] Department of Physics, The Hong Kong University of Science and Technology, Clear Water Bay, Kowloon, Hong Kong SAR
[2] Thrust of Advanced Materials, and Guangzhou Municipal Key Laboratory of Materials Informatics, The Hong Kong University of Science and Technology (Guangzhou), Guangdong, China
[3] Interdisciplinary Programs Office, The Hong Kong University of Science and Technology, Clear Water Bay, Kowloon, Hong Kong SAR
[4] Department of Mathematics, The Hong Kong University of Science and Technology, Clear Water Bay, Kowloon, Hong Kong SAR

Note: This paper is part of the 2024 JCP Emerging Investigators Special Collection.
[a)] **Present address:** Division of Physics and Astronomy, Graduate School of Science, Kyoto University, Kyoto, Japan.
[b)] zechenggan@ust.hk
[c)] **Author to whom correspondence should be addressed:** ruizhang@ust.hk

ABSTRACT

In living and synthetic active matter systems, the constituents can self-propel and interact with each other and with the environment through various physicochemical mechanisms. Among these mechanisms, chemotactic and auto-chemotactic effects are widely observed. The impact of (auto-)chemotactic effects on achiral active matter has been a recent research focus. However, the influence of these effects on chiral active matter remains elusive. Here, we develop a Brownian dynamics model coupled with a diffusion equation to examine the dynamics of auto-chemotactic chiral active droplets in both quasi-two-dimensional (2D) and three-dimensional (3D) systems. By quantifying the droplet trajectory as a function of the dimensionless Péclet number and chemotactic strength, our simulations well reproduce the curling and helical trajectories of nematic droplets in a surfactant-rich solution reported by Krüger *et al.* [Phys. Rev. Lett. **117**, 048003 (2016)]. The modeled curling trajectory in 2D exhibits an emergent chirality, also consistent with the experiment. We further show that the geometry of the chiral droplet trajectories, characterized by the pitch and diameter, can be used to infer the velocities of the droplet. Interestingly, we find that, unlike the achiral case, the velocities of chiral active droplets show dimensionality dependence: its mean instantaneous velocity is higher in 3D than in 2D, whereas its mean migration velocity is lower in 3D than in 2D. Taken together, our particle-based simulations provide new insights into the dynamics of auto-chemotactic chiral active droplets, reveal the effects of dimensionality, and pave the way toward their applications, such as drug delivery, sensors, and micro-reactors.

Published under an exclusive license by AIP Publishing. https://doi.org/10.1063/5.0207355

I. INTRODUCTION

Active matter systems consist of self-propelled units that can convert stored energy into mechanical motion.[1–3] Active matter research is driven by two major scientific questions. The first one is about the self-propulsion mechanism of individual units, which has led to a more comprehensive understanding of how microorganisms swim at low Reynolds numbers.[4–9] The second question is concerned with the mechanism underlying the collective motion (e.g., swarming and schooling) observed in cells, organisms, and animal herds. Exploring this question has led to significant theoretical advancements and model inventions.[10,11] Active matter has immense potential to impact various fields, including biology, materials science, and robotics.[12–16]

In biological systems, motile microorganisms often communicate with each other through signaling molecules and use various taxis mechanisms (gradient-driven migration) to perceive and survive in the environment.[17–20] For example, they can exhibit chemotaxis or auto-chemotaxis by navigating in the surroundings according to the gradient of certain external or self-generated

22 January 2025 20:28:18

Published under an exclusive license by AIP Publishing

chemical fields. These mechanisms are important for single cell dynamics, colony migration and aggregation, biofilm formation,[21–24] and quorum sensing.[25–28]

Artificial microswimmers can also exhibit chemotaxis or auto-chemotaxis through certain physicochemical processes ranging from nano to micro scale.[29] For example, certain colloidal particles can self-propel by generating a chemical gradient in their local environment.[30–33] Examples include Janus colloidal particles in hydrogen peroxide solution or under UV light[12,34,35] and self-propelled emulsion droplets in surfactant-rich aqueous solutions.[36,37] Notably, Ebbens, Campbell, and co-workers used dimers of Janus particles[38] and Janus particles coated by glancing angle evaporation method[39,40] to demonstrate a variety of self-propulsion trajectories showing chiral symmetry breaking. Suspensions of these particles exhibit intricate dynamics that are significantly influenced by the auto-chemotaxis.[41–44] Recent studies of the collective behaviors of auto-chemotactic particles include critical dynamics and characteristic length scaling law of population of diffusing agents and chemical fields,[45] self-caging of auto-chemotactic particles,[46] phase separation of active emulsion droplets,[47,48] and Janus colloidal doublets emergent in cycloidal trajectories.[49]

Elucidating the self-propelling behaviors of individual emulsion phoretic particles capable of chemotaxis is also an ongoing research effort.[50] Spherical symmetric droplets exhibit active Brownian motion.[1,51–55] When the dispersed phase is a nematic liquid crystal, Bahr, Maass, and co-workers have demonstrated that there is a cascade of spontaneous symmetry breaking, i.e., the self-propelled nematic droplets can exhibit circular motion in a surfactant solution well above the critical micelle concentration.[41,43,56–58] Interestingly, in unconfined, three-dimensional (3D) solutions, these active nematic droplets move in a helical trajectory; while in quasi-two-dimensional (2D) systems, they demonstrate a curling motion, with their average trajectory also displaying a curly pattern.[57] Similar helical or circular trajectories have also been observed in bacterial and artificial swimmers with structural asymmetry or near an interface, such as *E. Coli* and sea urchin sperms.[23,59,60]

The investigation of chiral active matter has garnered significant attention in recent years due to the broken time-reversal symmetry and the emergence of novel collective dynamics. Artificial microswimmers offer a convenient and controllable platform to understand chiral living microswimmers. Moreover, these man-made chiral active particles provide novel synthetic systems for potential applications, such as targeted therapeutic delivery and dynamic self-assembly.[61–64]

Modeling of auto-chemotactic droplets accounting for all the physicochemical details in simulations poses a challenge to date. Take the self-propelled nematic droplet in a surfactant-rich solution as an example, there is a cascade of spontaneous symmetry breaking that leads to the curling trajectory of the droplet.[65,66] One modeling approach involves solving the hydrodynamic equation, which accounts for the boundary condition on the droplet interface, and advection, diffusion, and solubilization of the surfactants. Through combined theoretical and numerical efforts, researchers have made progress in understanding the spontaneous locomotion.[67–70] However, the emergence of droplet chirality arises from their intricate internal structures,[52,54,55,71] making it computationally demanding, if not impossible, to elucidate using a full hydrodynamic approach. An alternative approach is to construct a minimal model that consists of a self-propelled, point, or disk/spherical particle. The minimal model offers a convenient means to incorporate intrinsic properties of droplets, such as chirality.[46,72–74]

In this work, therefore, we employ the particle-based approach to examine the versatile trajectories of auto-chemotactic chiral active droplets. We aim to address the following question: Given the complexity of the nematic droplet experiment, what are the minimum physical mechanisms/effects we should include to elucidate the curling and helical trajectories observed in 2D and 3D, respectively? Here, we hypothesize that chiral active motion, auto-chemotactic effect, and dimensionality are adequate to reproduce these trajectories.

To address the above question and to demonstrate our hypothesis, we couple active Brownian dynamics with a chemical field diffusion equation to investigate the dynamics of auto-chemotactic chiral active droplets. Our simulations successfully reproduce the two characteristic trajectories observed in the experimental observations of self-propelled nematic droplets in surfactant-rich aqueous solutions. We further adopt our model to examine how different physical parameters quantitatively impact the geometry of these trajectories. Specifically, we investigate how the strength of the chemotactic force, Péclet number, and dimensionality modify droplet kinetics in terms of its velocities and angular velocities. These analyses provide important insights into how chemical ingredients, such as chemotactic force and Péclet number, dictate the self-propelling dynamics of auto-chemotactic chiral active droplets, and offer a convenient and reliable model for the future study of chemical-mediated active matter.

II. MODEL

We model the dynamics of a self-propelled droplet in a chemical field by active Brownian dynamics simulations coupled with a diffusion equation. Specifically, a droplet of radius R is self-propelling at an intrinsic linear velocity of magnitude v_0, rotating with a time-dependent orientation (unit) vector $\hat{\boldsymbol{p}}$ at an angular velocity of ω_0[75] with a rotation axis $\hat{\boldsymbol{\tau}}$ that is always perpendicular to $\hat{\boldsymbol{p}}$. Therefore, $\hat{\boldsymbol{p}}$ and $\hat{\boldsymbol{\tau}}$ can be regarded as a reference frame of the droplet. The droplet is also subjected to a chemotactic force due to its self-generated chemical field [Fig. 1(a)]. In this work, we focus on negative chemotactic forces to correspond to the nematic droplet experiment.[57]

In this model, a point source located at the droplet's centroid emits certain chemicals at a rate of Q_0 with diffusivity D that produces a self-generated chemical gradient. We choose the droplet radius R, the intrinsic self-propelling speed v_0, and emitting rate Q_0 as the basic unit of length, time, and chemical source rate, respectively,

$$\boldsymbol{r} = \frac{\boldsymbol{r}^*}{R}, \qquad t = t^* \frac{v_0}{R}, \quad \text{and} \quad C = C^* \frac{v_0}{Q_0 R}. \tag{1}$$

It is, therefore, convenient to write the dimensionless equations of motion (Appendix A) by choosing $R = v_0 = Q_0 = 1$ as follows:

$$\frac{\mathrm{d}\boldsymbol{r}_p}{\mathrm{d}t} = \hat{\boldsymbol{p}} + \mathbf{F}_c, \tag{2}$$

$$\frac{\mathrm{d}\boldsymbol{\Theta}}{\mathrm{d}t} = \mathcal{R}\boldsymbol{\Theta}, \tag{3}$$

22 January 2025 20:28:18

Published under an exclusive license by AIP Publishing

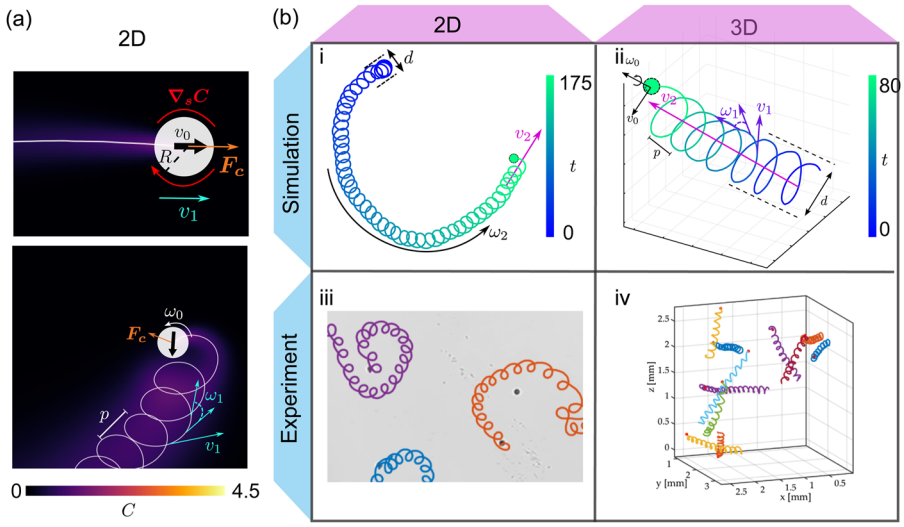

FIG. 1. Simulated trajectories of auto-chemotactic chiral active droplets. (a) Simulated trajectories in 2D. Top: in the linear case ($\Omega_0 = 0$), the chemotactic force $\mathbf{F}_c$ aligns with the droplet's active velocity vector $\mathbf{v}_0 = v_0\hat{\boldsymbol{p}}$. Bottom: in the chiral case ($\Omega_0 \neq 0$), the droplet exhibits a curling trajectory with a pitch p. The chemotactic force $\mathbf{F}_c$ is no longer aligned with $\mathbf{v}_0$. (b) Simulated 2D droplet trajectory (i) in comparison to the experimental trajectory (iii)[57] (permission granted by APS), and simulated 3D droplet trajectory (ii) in comparison to the corresponding experimental trajectory (iv)[57] (permission granted by APS). The emergent velocity v_2, emergent angular velocity ω_2, helical pitch p, and helical diameter d are graphically defined.

$$\frac{\partial C}{\partial t} = \frac{1}{\mathrm{Pe}}\nabla^2 C + \delta(\boldsymbol{r} - \boldsymbol{r}_p). \tag{4}$$

Equations (2) and (3) describe the over-damped Brownian motion of the active particle, where its body axes are described by the two orthogonal unit vectors, defined as $\boldsymbol{\Theta} = [\hat{\boldsymbol{p}}, \hat{\boldsymbol{\tau}}]^T$. A rotational matrix $\mathcal{R}$ rotates the droplet's major and minor axes $\hat{\boldsymbol{p}}$ and $\hat{\boldsymbol{\tau}}$ simultaneously at an angular velocity $\boldsymbol{\omega} = \Omega_0\hat{\boldsymbol{\tau}} + \sqrt{2/\Gamma}\boldsymbol{\xi}(t)$, where $\Omega_0 = R\omega_0/v_0$ is the dimensionless angular velocity, Γ is the dimensionless persistence length of the droplet, and $\boldsymbol{\xi}(t)$ is a rotational white noise with zero mean, i.e., $\langle\boldsymbol{\xi}(t)\rangle = \mathbf{0}$. In 2D, $\boldsymbol{\xi}(t) = \xi(t)\hat{z}$ and $\langle\xi(t)\xi(t')\rangle = \delta(t - t')$; and in 3D, $\langle\xi_\mu(t)\xi_\nu(t')\rangle = \delta_{\mu\nu}\delta(t - t')$,[66,75,76] where the Greek subindices μ and ν denote the Cartesian coordinates x, y and z. It is worth remarking that in 2D, the droplet moves within the xy-plane, meaning that the unit vector $\hat{\boldsymbol{\tau}}$ is always aligning with $\boldsymbol{\xi}$, which is along the z-axis. However, this is not the case in 3D. Numerically, we evaluate the rotation of the droplet using the Rodrigues formalism (Appendix B). Finally, Eq. (4) describes the evolution of the chemical field due to the droplet's emission and free diffusion. Note that, for the 2D case, there are many alternative experimental setups, such as droplets confined by plates or at an interface. In our 2D model, we consider both the droplets and the chemical field to be confined to the xy-plane. Thus, we can simply solve the 2D diffusion equation (instead of 3D with certain boundary/interface conditions in z) to obtain an effective 2D chemical field evolution. To model the quasi-2D case in which the droplet is confined to a liquid interface, we can modify Eq. (4) by including a decay term to account for the unconfined diffusion of the chemical field in the z-dimension: $\frac{\partial C}{\partial t} = \frac{1}{\mathrm{Pe}}\nabla^2 C + \delta(\boldsymbol{r} - \boldsymbol{r}_p) - \beta C$ with β being a constant decay rate.

The system can be described by four dimensionless numbers:

(1) The *chemotactic constant*, Λ: it sets the scale of the chemotactic force $\mathbf{F}_c$ that is proportional to the average of the tangential gradient of the chemical concentration on the droplet surface,[56,68,77]

$$\mathbf{F}_c = -\frac{\Lambda}{A}\oint_S \nabla_s C dS, \tag{5}$$

where ∇_s is the surface-gradient operator defined as $\nabla_s = (\mathbf{I} - \mathbf{nn}) \cdot \nabla$, with $\mathbf{I}$ being the identity tensor and unit vector $\mathbf{n}$ denoting the surface normal. The surface area $A = 2\pi R$ and $A = 4\pi R^2$ in 2D and 3D, respectively.

(2) The *persistence length*, $\Gamma = l_p/R$: it is a reduced characteristic length scale in which a droplet travels before it changes its orientation. Here, we only consider the rotational noise because it dominates the particle dynamics.[78,79] In Appendix C, we show that the chiral droplet trajectories with and without the translational noise are similar in both 2D and 3D.

(3) The *chirality*, $\Omega_0 = R\omega_0/v_0$: it acts as a constant angular torque along $\hat{\boldsymbol{\tau}}$ to rotate the orientation vector $\hat{\boldsymbol{p}}$. In 2D, $\hat{\boldsymbol{\tau}}$ is fixed at the z-axis; thereby, $\hat{\boldsymbol{p}} = (\cos\theta, \sin\theta)$. Equation (3) can be reduced to

$$\frac{\mathrm{d}\theta}{\mathrm{d}t} = \Omega_0 + \sqrt{\frac{2}{\Gamma}}\xi(t). \tag{6}$$

In the 3D case, it is more convenient to use the rotational operator $\mathcal{R}$ to perform the rotations on $\boldsymbol{\Theta}$ in 3D, which can be accurately calculated by the Rodrigues formula[80] in the particle frame (see Appendix B for detailed formulations).

22 January 2025 20:28:18

Published under an exclusive license by AIP Publishing

(4) The active *Péclet number*, $\mathrm{Pe} = Rv_0/D$: it is the ratio of the self-propelling velocity of the droplet to the diffusion rate of the emitted chemical. It measures the relative influence of the droplet's motion and chemical diffusion on its behavior. Alternatively, it can be interpreted as a measure of the droplet's size by selecting the characteristic time scale as R/v_0.[41,69,81]

We employ the Euler–Maruyama scheme to numerically integrate Eqs. (2) and (3). We also incorporate the immersed boundary method and finite difference method (grid-based) to evaluate Eq. (4) (Appendix D). Finally, to validate the accuracy of our grid-based solver, we compare it to a mesh-free Green's function method that provides higher accuracy for larger values of Pe and Λ (Appendix E). The effects of persistence length and chirality on the interactions between chiral active particles and the complex environment have been discussed in a previous work.[62] In this work, we choose to focus on the impact of the chemotactic effect by fixing $\Omega_0 = 1$ and $\Gamma = 500$.

III. RESULTS

A. The curling and helical trajectory

One of the unique features of auto-chemotactic chiral active droplets is their curling trajectories in 2D and helical trajectories in 3D, which have been reported in the nematic droplet experiment.[56,57] Our simulation results match very well with the experimentally observed trajectories [Fig. 1(b)]. In what follows, we focus on characterizing the droplet dynamics. Their motion can be described by an instantaneous linear velocity v_1 and an instantaneous angular velocity ω_1 [Fig. 1(a)]. In addition, the droplet motion can also be described by an emergent (migration) velocity v_2 characterizing its average displacement or migration as a function of time [Fig. 1(b)]. In 2D, there is an emergent angular velocity ω_2 that characterizes the curling trajectory of the droplet. Associated with these curling or helical trajectories, a pitch p and a helical diameter d can also be introduced to describe the geometry of droplet trajectories in both 2D and 3D (Fig. 1).

In the experiment, the chiral structure of the droplet's trajectory arises from a three-step process of spontaneous symmetry breaking. In the first step, the droplet acquires self-propelling motion caused by a Marangoni flow on the droplet's surface.[46,51,56] In our model, this is modeled by a constant self-propelling velocity v_0 [Fig. 1(a)]. In the second step, the droplet's motion gains a rotational component from the misposition of the topological defect,[57] and this is modeled as a constant angular velocity ω_0 [Fig. 1(a)]. In the third step, the filled chemical trail further breaks the symmetry of the propelling direction, hence causing the trajectory to form a curling or helical pattern.[54,57,71,82] This effect is modeled by a chemical field diffusion and a negative auto-chemotactic effect [Fig. 1(b)].

It is worth emphasizing that a static angular velocity alone is insufficient to explain the emergence of the helical trajectory in 3D. In the absence of an out-of-plane component in the force acting on the droplets, as is the case in 2D, the droplet's trajectory will be

22 January 2025 20:28:18

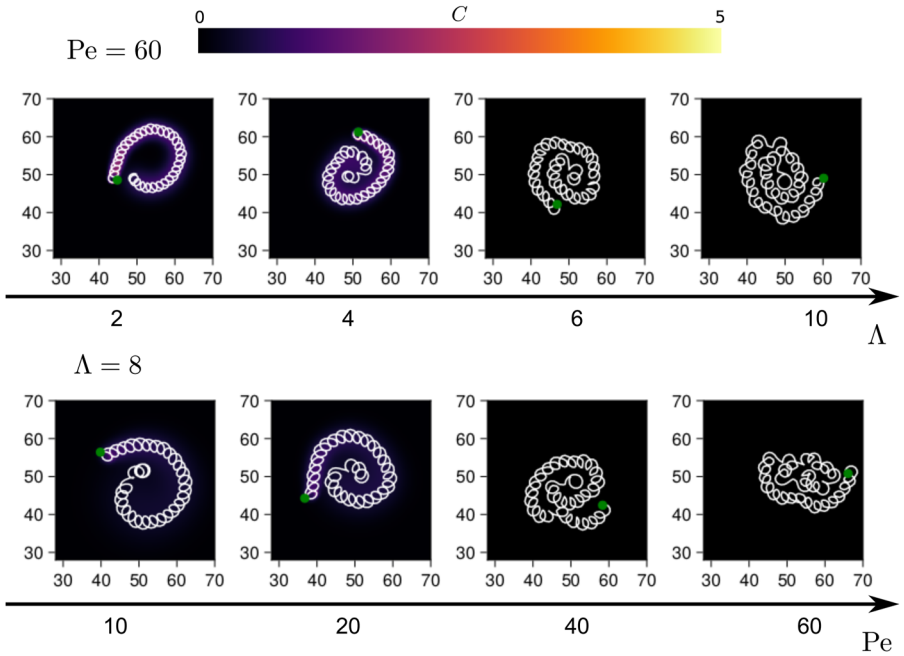

FIG. 2. Curling trajectories in 2D. Droplet trajectories with varying values of Λ at fixed Pe = 60 (top) and varying values of Pe at fixed $\Lambda = 8$ (bottom). The trajectory gradually changes from the curling mode to an unstable mode as Λ (top) or Pe (bottom) increases. Background color shows the chemical field C and Green dots indicate the final positions of the droplet. The mesh-free method is used to produce trajectories for $\mathrm{Pe} > 40$ and $\Lambda > 6$.

Published under an exclusive license by AIP Publishing

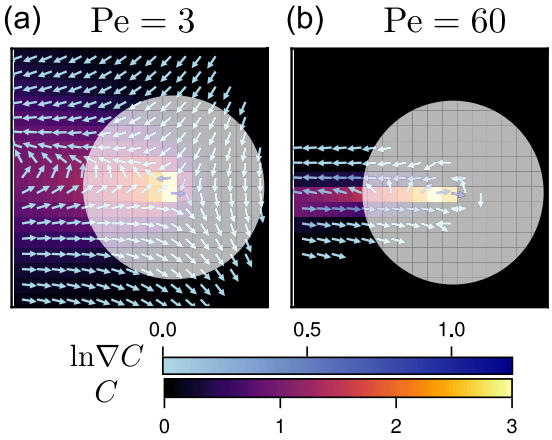

FIG. 3. Chemical gradient field in 2D. The concentration field C (background color) and its gradient ∇C (the vector field) for a linear auto-chemotactic active droplet with Pe = 3 (a) and Pe = 60 (b) at the same $\Lambda = 4$.

confined to the plane normal to $\hat{\boldsymbol{\tau}}$ and exhibit a curling motion.[57] An out-of-plane noise in the force is required for the droplet to develop a persistent displacement propulsion along the third dimension.[55,57,82]

In 2D, the curling trajectory may become irregular when Pe or Λ becomes too large:[68,77] the trajectory can transition from a periodic curling structure to a more irregular shape when $\Lambda > 6$ and Pe > 40 (Fig. 2). This is attributed to the increasing repelling force from the chemical trail. The chemotactic force is closely associated with Λ [which scales the interaction directionally, Eq. (5)] and Pe [which determines the distribution of the chemical field, Eq. (E2)]. At high Pe, the self-propelled speed of the droplet is much faster than the diffusion of the chemical field. In this regime, the droplet tends to leave behind a thin and distinct trail due to the relatively slow diffusion (Fig. 3). Consequently, when a droplet encounters its own trail, it experiences a strong chemotactic force resulting from the significant gradient present. Therefore, the droplet becomes increasingly difficult to pass through smoothly as Λ or Pe increases.[46] However, the helical trajectory in 3D remains stable for large Pe and Λ (Fig. 4). This is because the extra degree of freedom allows the droplet to move along the $\hat{\boldsymbol{\tau}}$-axis, preventing a strong repulsion from the trail of the chemical.

B. Mean velocities of chiral and linear auto-chemotactic droplets in 2D and 3D

We quantify the mean instantaneous velocity of chiral ($\Omega_0 \neq 0$) and linear ($\Omega_0 = 0$) droplets as $\langle v_1 \rangle$ and $\langle v_1 \rangle_{\text{linear}}$, respectively. By comparing the two quantities, we can elucidate the effect of chirality on the dynamics of auto-chemotactic active droplets. We first find that both $\langle v_1 \rangle$ and $\langle v_1 \rangle_{\text{linear}}$ increase monotonically with an increase in Λ, which is consistent with our expectation that Λ scales the magnitude of $\mathbf{F_c}$ [Eq. (5)], thereby linearly scaling the instantaneous velocity [Figs. 5(a) and 5(c)]. When Pe $\lesssim 10$, the two mean instantaneous velocities grow rapidly as Pe increases [Figs. 5(b) and 5(d)]. Note that the smaller Pe is, the more homogeneous the chemical field becomes, and this can lead to the smaller chemotactic force acting on the droplet.[68] Therefore, as Pe $\to 0$, both $\langle v_1 \rangle$ and $\langle v_1 \rangle_{\text{linear}}$

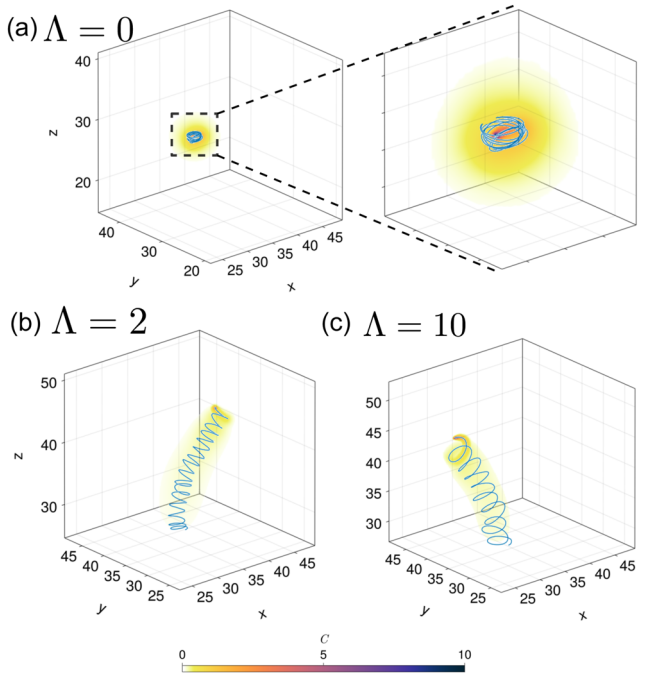

FIG. 4. Droplet trajectories in 3D (a)–(c) The droplet trajectory and the concentration field for $\Lambda = 0$ (a), 2 (b), and 10 (c) at Pe = 20. The background color shows the chemical concentration field C. The inset in (a) is a zoomed-in view of the trajectory. The pitch p of the helical trajectory increases as Λ increases.

approach to $v_0 = 1$, the intrinsic self-propelling velocity. When Pe increases from 10, both $\langle v_1 \rangle$ and $\langle v_1 \rangle_{\text{linear}}$ reach a plateau [Figs. 5(b) and 5(d)] due to the thinning of the chemical tail, resulting in a reduced contribution from the tangential gradient [Fig. 3(b)]. Similar droplet behaviors as a function of Pe are also reported in other fully hydrodynamic models.[68,83,84]

We next examine the dimensionality dependence of droplet velocities. For linear/achiral active droplets, their mean velocities, $\langle v_1 \rangle_{\text{linear}}$s, are insensitive to system dimension [Figs. 5(c) and 5(d)]. By contrast, chiral active droplets exhibit nontrivial dimensionality dependence. Specifically, we find that $\langle v_1 \rangle$ is smaller in 2D than in 3D [Figs. 5(a) and 5(b)]. In 2D, the droplet's trajectory is confined to the xy-plane,[56,57,73] and it experiences a periodic push and pull by the chemical trail (Fig. 6). This effectively impedes droplet propulsion on average. In 3D, however, the droplet is pushed by a more uniform repulsive chemotactic force toward the third direction to form a helical trajectory (Fig. 6), leading to a relatively higher $\langle v_1 \rangle$. In a similar phenomenon, it can be rigorously proved that microparticles will always transport slower in a periodic potential than in a uniform potential.[85] The difference in dimensionality dependence between achiral and chiral active droplets implies that there is an interesting interplay between chirality and dimensionality.

We further compare chiral and achiral droplets. We find that $\langle v_1 \rangle / \langle v_1 \rangle_{\text{linear}} < 1$ in both 2D and 3D [Figs. 5(e) and 5(f)]. For linear active droplets, the chemotactic force is parallel with the droplet velocity, serving to accelerate droplet self-propulsion [Fig. 1(a)]. For chiral active droplets, such force is not aligned

22 January 2025 20:28:18

Published under an exclusive license by AIP Publishing

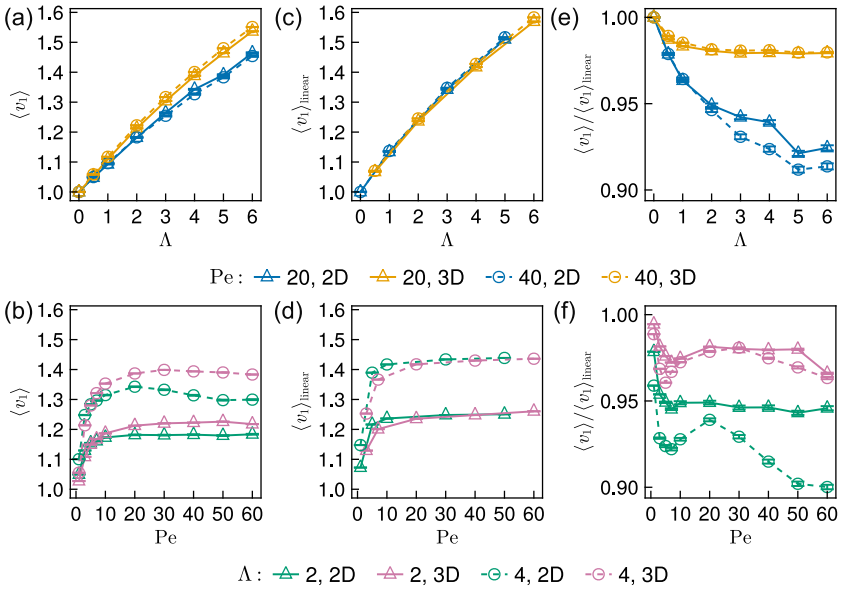

FIG. 5. Mean instantaneous velocities of auto-chemotactic chiral active droplets. (a)–(d) Mean instantaneous velocities $\langle v_1 \rangle$ for chiral droplets ($\Omega_0 \neq 0$) and $\langle v_1 \rangle_{\text{linear}}$ for linear droplets ($\Omega_0 = 0$). (e) and (f) The ratio $\langle v_1 \rangle / \langle v_1 \rangle_{\text{linear}}$. (a), (c), and (e) $\Lambda \in [0, 6]$ with fixed Pe = 20, 40. (b), (d), and (f) Pe $\in [0, 60]$ with fixed $\Lambda = 2, 4$.

with the droplet velocity, thereby providing less acceleration effect [Fig. 1(a)]. Moreover, $\langle v_1 \rangle / \langle v_1 \rangle_{\text{linear}}$ decreases from 1 when Λ or Pe increases [Figs. 1(e) and 1(f)], further supporting the argument that the droplet velocity is dictated by the chemotactic force, as the chemotactic effect is pronounced when Λ or Pe is large. We also observe that $\langle v_1 \rangle / \langle v_1 \rangle_{\text{linear}}$ is sensitive to large Pe and Λ values in 2D but much less sensitive to these parameters in 3D. This difference can be understood by the unstable motion in 2D, comparing with the stable helical motion in 3D even at higher Pe and Λ values. Notably, the variation of v_1 is significantly larger in 2D compared to 3D (Fig. 6).

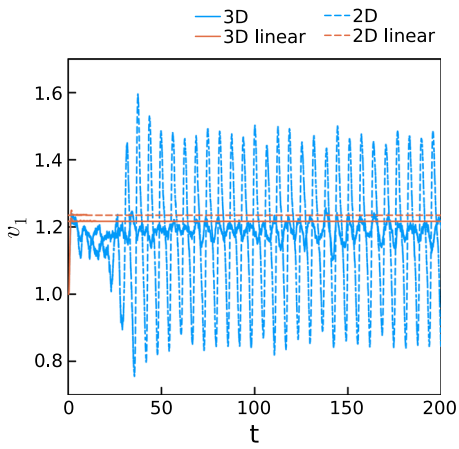

FIG. 6. Instantaneous droplet velocities. Instantaneous velocity v_1 of chiral (blue) and linear (orange) auto-chemotactic droplets in 2D (dashed) and 3D (solid) as a function of time.

C. Emergent droplet behaviors

The behavior of the emergent velocity, namely, $\langle v_2 \rangle$ [Fig. 1(bi-ii)], follows a similar trend to $\langle v_1 \rangle$ as a function of Pe and Λ. However, $\langle v_2 \rangle$ is smaller in 3D than in 2D [Figs. 7(a) and 7(b)], which appears to be in contrary to the behavior of $\langle v_1 \rangle$. This can be explained by the distinct nature of the emergent trajectories in 2D and 3D. In 2D, the droplet's trajectory is a curling pattern due to the confinement. This results in a higher emergent velocity at the price of a slower $\langle v_1 \rangle$. On the other hand, in 3D, the emergent trajectory takes a helical shape and slowly migrates in the third dimension. This leads to a smaller $\langle v_2 \rangle$ while having a higher $\langle v_1 \rangle$. The contrasting behavior of $\langle v_2 \rangle$ between 2D and 3D systems highlights the influence of dimensionality on the emergent dynamics of chemotactic systems. Understanding these differences is crucial in characterizing and predicting the behavior of active particles in different spatial dimensions.[67,82,86]

Moreover, the angular velocity ω_1 remains nearly a constant across all cases [Figs. 7(c) and 7(d)]. This can be attributed to the absence of external torque in our equation of motion [Eq. (3)], $\omega_1 \cong \omega_0$. It is worth noting that the fluctuations of ω_1 revealed by the FFT analysis (Appendix H) are larger in 2D than in 3D. This is consistent with the fact that 2D droplets experience more fluctuations (Fig. 6).

22 January 2025 20:28:18

Published under an exclusive license by AIP Publishing

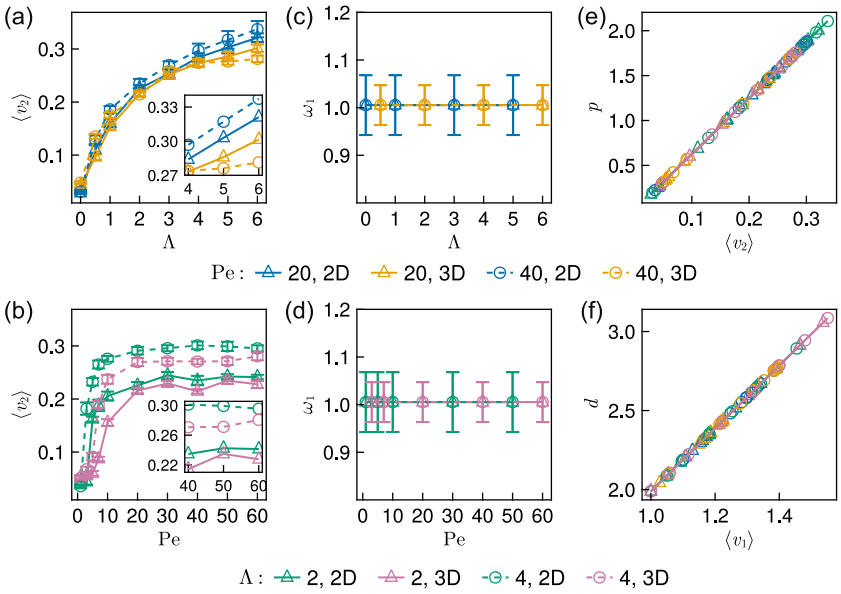

FIG. 7. Emergent velocities and angular velocities of auto-chemotactic chiral active droplets. (a) and (b) The emergent velocity $\langle v_2 \rangle$ as a function of Λ (a) and Pe (b). (c) and (d) Angular velocity ω_1 obtained from fast Fourier transform (FFT) analysis as a function of Λ (c) and Pe (d). (e) and (f) Pitch p of the emergent trajectory (e) and the helical diameter (f) are linearly related to $\langle v_2 \rangle$ and $\langle v_1 \rangle$, respectively, regardless of dimensionality.

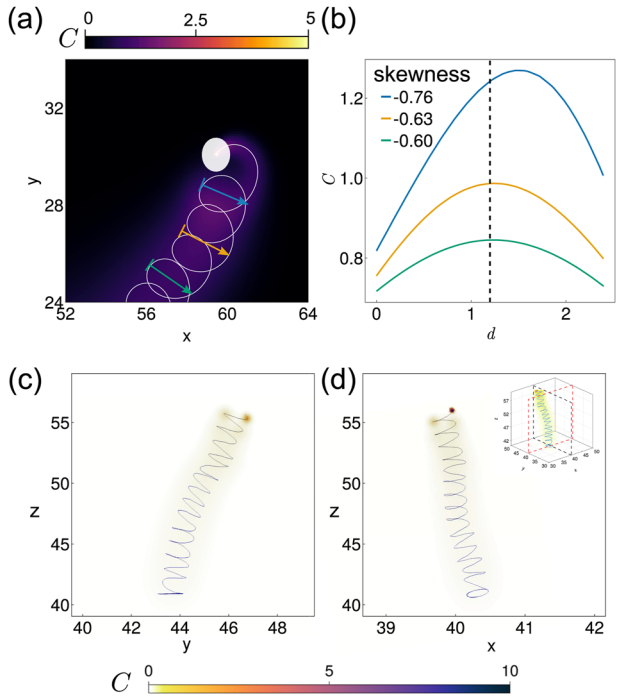

FIG. 8. More details of the concentration field. (a) and (b) Concentration field (b) along the diameter d of the curling trajectory at three different positions indicated in (a). The black dashed line in (b) represents the center of the curling trajectory. (c) and (d) Cross section of the concentration field along the center of the helical trajectory in the yz plane (black dashed box in the inset) and xz plane (red dashed box in the inset).

The pitch of the curling and helical trajectory can be represented as $p = \langle v_2 \rangle T = \langle v_2 \rangle \frac{2\pi}{\omega_1}$. Since ω_1 is a constant in both 2D and 3D, p is proportional to $\langle v_2 \rangle$. Figure 7(e) shows that there is a linear relationship between p and $\langle v_2 \rangle$.

Upon analyzing the trajectories in both 2D and 3D, we measure the helical diameter of the curling trajectory as $d = 2\frac{\langle v_1 \rangle}{\omega_1}$, as illustrated in Fig. 1. Since ω_1 is a constant, d is proportional to $\langle v_1 \rangle$ [Fig. 7(f)]. Similar to p, we again find a linear mapping between d and $\langle v_1 \rangle$. Therefore, the dynamics of the auto-chemotactic chiral active droplets can be conveniently inferred by their trajectory geometries.

Our simulation also provides useful details to elucidate the emergent chirality of the 2D droplet trajectories. By measuring the concentration field C along the helical diameter direction [Fig. 8(a)], we find that the C field shows a bias toward the right-hand side of the migration direction by exhibiting a negative skewness [Fig. 8(b)]. In fact, the counter-clockwise moving droplet periodically crosses its own trail on the right-hand side of its mean migration direction. This effectively increases the C field on the right-hand side and gives rise to a repulsive force toward to the left-hand size. Thereby, the droplet tends to migrate toward left with respect to its mean migration direction. This symmetry breaking in the C field is not observed in 3D [Figs. 8(c) and 8(d)], as the droplet spirally migrates without crossing its own trace.

The emergent angular velocity ω_2 is measured as a function of Pe and Λ (Fig. 9). As expected, the higher the chemotactic effect is, the higher ω_2 is. Interestingly, ω_2 is more sensitive to Λ than to Pe. Because Λ directly scales the chemotactic force, whereas Pe sets the diffusion rate of the chemical. Again, similar to the Pe dependence of droplet velocities $\langle v_1 \rangle$ and $\langle v_2 \rangle$, ω_2 also exhibits a plateau when Pe $\gtrsim$ 20. For large Pe and Λ, the irregular droplet trajectories render

22 January 2025 20:28:18

Published under an exclusive license by AIP Publishing

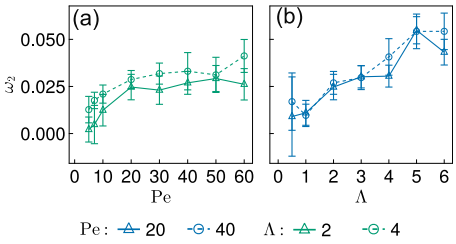

FIG. 9. Emergent angular velocity ω_2 of the curling trajectory in 2D. (a) and (b) ω_2 for Pe $\in [0, 60]$ with fixed $\Lambda = 2, 4$ (a) and for $\Lambda \in [0, 6]$ with fixed Pe = 20, 40 (b).

the measurement of ω_2 increasingly difficult and give rise to large error bars.

IV. DISCUSSION

In this work, we use active Brownian dynamics coupled with a chemical field diffusion to model auto-chemotactic chiral active droplets, utilizing the immersed boundary method (IBM) as the numerical approach. This approach replaces the delta function with a regularized kernel function for grid-based simulations. By employing this model, we successfully recapitulate the curling and helical trajectories exhibited by the chiral auto-chemotactic droplets in both 2D and 3D environments, matching well with the experimental observations.[57] In a recent work by Li and Koch, a 2D multi-phase fluid approach was employed to model a 2D self-propelled compound droplet. The symmetry breaking of the two fluid compartments can lead to chiral trajectories similar to the curling trajectory discussed here.[77] However, the emerging chirality was not reported in that model.[77]

Note that chiral trajectories have also been observed in various Janus colloidal particles[38–40,49] and in isotropic oil droplets.[87] In these systems, however, the chirality is either unstable or there is no chemotactic effect. As a result, stable curling or helical structure is absent in these trajectories. By contrast, in the liquid crystal experiment, the chirality of the droplet motion due to a spontaneous symmetry breaking is stable and there is a negative chemotactic effect.[57] In our model, an intrinsic chirality is implemented in the equation of motion for the droplet via introducing an intrinsic nonzero angular velocity Ω_0 in Eq. (3). By including a negative chemotactic effect, our simulation reproduces the curling or helical trajectories. Our simulation further suggests that the interplay of the intrinsic chirality of the droplet and its negative chemotactic effect can give rise to the emergent, secondary chirality in its trajectory in 2D. In the future, we will extend our current model to switchable (unstable) chirality. Note that if the auto-chemotactic effect is positive (attraction), we expect that both 2D and 3D droplets will exhibit self-trapping, cyclic trajectories and lose the helical structure, as is similar to a previous work, in which the diffusion of the chemical trail was not considered.[24]

The mean velocity of the chemotactic droplets increases as Pe and Λ increase. Comparing 2D and 3D cases, the mean velocity is higher in 3D due to an additional degree of freedom. However, there is a transition where the mean linear velocity is higher in 2D below a certain threshold but higher in 3D above that threshold. The mean velocity is consistently smaller than the mean linear velocity, indicating a slowing effect caused by the periodic chemotactic force.

Furthermore, the emergent velocity $\langle v_2 \rangle$ increases with higher chemotactic force, but it is smaller in 3D than in 2D. This is because the emergent trajectories in 2D exhibit a curling pattern, resulting in higher $\langle v_2 \rangle$ due to confinement, while in 3D, the trajectories take a helical form and migrate slowly, leading to lower $\langle v_2 \rangle$ despite higher $\langle v_1 \rangle$. In both 2D and 3D, the angular velocity ω_1 remains to be a constant, and the pitch of the trajectories is proportional to $\langle v_2 \rangle$. In addition, the curling trajectory in 2D displays a higher degree of symmetric breaking, resulting in a more pronounced emergent chiral structure compared to the 3D case.

The challenging nature of simulating (auto)chemotactic droplets, especially when considering their complex coupling of Stokes flow, chemical diffusion, and internal structure, has led to the development of various models in the literature (Table I). These models can generally be classified into two approaches: full hydrodynamic simulations and particle-based simulations. Each approach employs different numerical methods and emphasizes various aspects of the dynamic behavior observed experimentally.

Hydrodynamic simulation methods, such as multi-phase fluids[69,77,88] and rigid disks with accurate boundary conditions,[68]

TABLE I. List of models in (auto) chemotactic droplets.

	Dimension	Chirality	(Auto) chemotaxis	Self-interaction	Method
Hu *et al.*[68]	2D	×	Auto-chemotaxis	✓	Disk with BC
Morozov and Michelin[69]	2D	×	Auto-chemotaxis	✓	Multi-phase fluid
Li and Koch[77]	2D	✓ (spontaneous)	Auto-chemotaxis	✓	Multi-phase fluid
Kulkarni *et al.*[88]	2D and 3D	×	Auto-chemotaxis	✓	Multi-phase fluid
Maity and Burada[89]	3D	✓ (intrinsic)	Chemotaxis	×	Chiral squirmers
Saha *et al.*[90]	2D	×	Chemotaxis	×	Particle-based
Stürmer *et al.*[91]	2D	×	Chemotaxis	×	Particle-based
Hokmabad *et al.*[46]	2D and 3D	×	Auto-chemotaxis	×	Particle-based
Ziepke *et al.*[42]	2D	×	Auto-chemotaxis	✓	Particle-based
Our model	2D and 3D	✓ (intrinsic)	Auto-chemotaxis	✓	Particle-based

22 January 2025 20:28:18

Published under an exclusive license by AIP Publishing

are optimized to capture the complete hydrodynamic interactions. These methods represent the intricate interplay between fluid flow, droplet motion, and chemical gradients. They are particularly useful for investigating the role of hydrodynamics in the behavior of (auto)chemotactic droplets such as how chiral symmetry is spontaneously broken due to hydrodynamic interactions.[87,92]

On the other hand, particle-based simulation models, such as phenomenological models of self-propelled point particles with chemotactic interactions,[42,46,90,91] offer advantages in terms of generalizability to 3D systems and the inclusion of chirality properties. In auto-chemotaxis, these models often simplify the droplets as point sources or sinks, neglecting their self-interaction as the singularity in the gradient. As a result, they are more commonly used for studying the collective behavior of multiple droplets rather than individual droplets.

Our phenomenological, particle-based model incorporates chiral effects and self-interaction, distinguishing it from other existing models (Table I). Our model includes self-interaction for a single droplet and evolving the chemical field in both 2D and 3D. This feature provides a more detailed understanding of the chemical gradients surrounding the droplets, offering useful insights into the impact of the chemical environment and intrinsic chirality on droplet dynamics.

As such, our work presents a convenient particle-based simulation model to phenomenologically study the interplay of multiple physical effects in active droplet dynamics. We have provided new insights into the effects of chirality and dimensionality on chemotactic active droplets. In future work, we will incorporate hydrodynamic effects and extend the study of single droplet dynamics to their collective behaviors, and positive auto-chemotactic effects will also be examined.

ACKNOWLEDGMENTS

R.Z. acknowledged financial support from the Research Grants Council of Hong Kong SAR (Grant No. 26302320). Z.G. acknowledged financial support from the Natural Science Foundation of China (Grant No. 12201146), the Natural Science Foundation of Guangdong (Grant No. 2023A1515012197), and the Guangzhou-HKUST(GZ) Joint Funding Program (Grant No. 2023A03J0003 and 2024A03J0606). The simulation was conducted using the HKUST Central High-Performance Computing Cluster (HPC3).

AUTHOR DECLARATIONS

Conflict of Interest

The authors have no conflicts to disclose.

Author Contributions

Chung Wing Chan: Formal analysis (lead); Investigation (lead); Methodology (lead); Writing – original draft (lead); Writing – review & editing (equal). **Zheng Yang**: Investigation (supporting); Writing – review & editing (equal). **Zecheng Gan**: Methodology (equal); Supervision (equal); Writing – review & editing (equal). **Rui Zhang**: Conceptualization (equal); Funding acquisition (equal); Project administration (equal); Supervision (equal); Writing – original draft (equal); Writing – review & editing (equal).

DATA AVAILABILITY

The data that support the findings of this study are available from the corresponding author upon reasonable request.

APPENDIX A: NON-DIMENSIONLESS EQUATIONS OF THE MODEL

We consider a self-propelling and self-rotating droplet with a radius of R, moving at a linear velocity v_0 and an angular velocity ω_0.[75] Certain chemical is emitted from the droplet's centroid at a rate of Q_0 and diffusivity D, creating a self-generated chemical gradient. This gradient leads to a negative chemotactic force $\boldsymbol{F}_c^*$ acting on the droplet from its environment,[46,72,73]

$$\frac{d\boldsymbol{r}_p^*}{dt^*} = v_0\hat{\boldsymbol{p}} - \boldsymbol{F}_c^*, \tag{A1}$$

$$\frac{d\hat{\boldsymbol{p}}}{dt^*} = \left(\omega_0\hat{\boldsymbol{\tau}} + \sqrt{2D_r}\boldsymbol{\xi}(t)\right) \times \hat{\boldsymbol{p}}, \tag{A2}$$

$$\frac{d\hat{\boldsymbol{\tau}}}{dt^*} = \left(\omega_0\hat{\boldsymbol{\tau}} + \sqrt{2D_r}\boldsymbol{\xi}(t)\right) \times \hat{\boldsymbol{\tau}}, \tag{A3}$$

$$\frac{\partial C^*}{\partial t^*} = D\nabla^{*2}C^* + \delta(\boldsymbol{r}^* - \boldsymbol{r}_p^*)Q_0, \tag{A4}$$

where $\hat{\boldsymbol{\tau}}$ is the rotational axis, which is always perpendicular to $\hat{\boldsymbol{p}}$.

APPENDIX B: 3D ROTATION

In 3D, we fix the relative configuration of $\boldsymbol{\Theta} = [\hat{\boldsymbol{p}}, \hat{\boldsymbol{\tau}}]^T$ such that

$$\frac{d\hat{\boldsymbol{p}}}{dt} = \left(\Omega_0\hat{\boldsymbol{\tau}} + \sqrt{\frac{2}{\Gamma}}\boldsymbol{\xi}(t)\right) \times \hat{\boldsymbol{p}}, \tag{B1a}$$

$$\frac{d\hat{\boldsymbol{\tau}}}{dt} = \left(\Omega_0\hat{\boldsymbol{\tau}} + \sqrt{\frac{2}{\Gamma}}\boldsymbol{\xi}(t)\right) \times \hat{\boldsymbol{\tau}}. \tag{B1b}$$

Here, $\hat{\boldsymbol{p}}$ and $\hat{\boldsymbol{\tau}}$ are under the same rotation due to the chirality $\Omega_0\hat{\boldsymbol{\tau}}$ and noise $\sqrt{2/\Gamma}\boldsymbol{\xi}(t)$. Instead of performing a small rotation about each axis at a time, it is advisable to perform a rotation directly about an axis defined by a vector $\boldsymbol{\omega}$,[80,93]

$$\boldsymbol{\omega} = (\omega_x, \omega_y, \omega_z) = \left(\frac{\Delta\theta_x}{\Delta t}, \frac{\Delta\theta_y}{\Delta t}, \frac{\Delta\theta_z}{\Delta t}\right), \tag{B2}$$

with the angular increment,

$$\Delta\theta = \Delta t|\omega| = \sqrt{(\Delta\theta_x)^2 + (\Delta\theta_y)^2 + (\Delta\theta_z)^2}. \tag{B3}$$

This is exactly the rotation acting on the particle, where $\Delta\theta_\mu = \Omega_0\hat{\tau}_\mu + \sqrt{2/\Gamma}\boldsymbol{\xi}_\mu(\Delta t)$. Such rotation matrix $\mathcal{R}$ can be written as the exponential of the skew-symmetric matrix $\boldsymbol{\theta}_\times$,

22 January 2025 20:28:18

Published under an exclusive license by AIP Publishing

$$\mathcal{R}(\Delta\theta) = e^{\boldsymbol{\theta}_\times} = \mathbb{I} + \sum_{n=1}^{+\infty} \frac{1}{n!}\boldsymbol{\theta}_\times^n, \tag{B4}$$

where

$$\boldsymbol{\theta}_\times = \begin{bmatrix} 0 & -\Delta\theta_z & \Delta\theta_y \\ \Delta\theta_z & 0 & -\Delta\theta_x \\ -\Delta\theta_y & \Delta\theta_x & 0 \end{bmatrix}. \tag{B5}$$

Because of the properties of $\boldsymbol{\theta}_\times$, namely, $\boldsymbol{\theta}_\times^3 = -\Delta\theta^2\boldsymbol{\theta}_\times$, it can be written as

$$\mathcal{R}(\Delta\theta) = e^{\boldsymbol{\theta}_\times} = \mathbb{I} + \frac{\sin\Delta\theta}{\Delta\theta}\boldsymbol{\theta}_\times + \frac{1-\cos\Delta\theta}{\Delta\theta^2}\boldsymbol{\theta}_\times^2.$$

This is the Rodrigues formula[80] for the rotation of an angle $\Delta\theta$ around a direction $\boldsymbol{\omega}$ that is exactly the rotation of the axes of the particle reference frame due to a rotational noise term of $\boldsymbol{\xi}$ and active torque Ω.

APPENDIX C: TRANSLATIONAL NOISE

To show the role of the translational noise, we introduce a noise term in Eq. (2) as

$$\frac{\mathrm{d}\boldsymbol{r}_p}{\mathrm{d}t} = \hat{\boldsymbol{p}} + \mathbf{F_c} + \sqrt{\frac{2}{\Gamma_t}}\boldsymbol{\eta}(t). \tag{C1}$$

Similar to the rotational noise $\boldsymbol{\xi}(t)$, the translational noise $\boldsymbol{\eta}(t)$ also has zero mean and satisfies $\langle \eta_\mu(t)\eta_\nu(t')\rangle = \delta_{\mu\nu}\delta(t-t')$. Figure 10 shows that the droplet trajectory is similar regardless of the presence of the translational noise. Therefore, throughout the main text, we set $\Gamma_t = 0$, and then, Eq. (C1) reduces to Eq. (2).

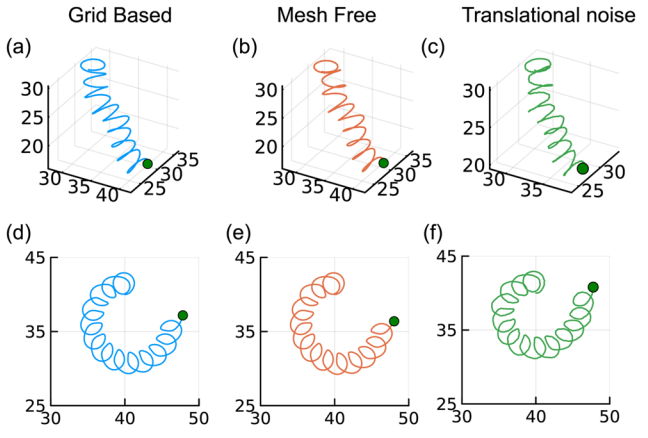

FIG. 10. Comparison of the two numerical methods and the effect of translational noise. (a)–(c) Droplet trajectories in 3D with Pe = 20 and $\Lambda = 5$ calculated using grid-based (a) and mesh-free method (b) and (c). (d)–(f) Droplet trajectories in 2D with Pe = 40 and $\Lambda = 4$ calculated using grid-based (d) and mesh-free methods (e) and (f). In 3D, a rotational noise level corresponding to $\Gamma = 500$ is applied, while in 2D, no rotational noise ($\Gamma = 0$) is introduced. An additional translational noise $\Gamma_t = 500$ is applied to (c) and (f). Green dots show the final positions of the droplets.

APPENDIX D: IMMERSED BOUNDARY METHOD (IBM)

To simulate droplet behavior in a chemical environment, we integrate the Langevin and diffusion equations numerically. Since the Langevin equation characterizes particle dynamics, while the diffusion equation for the chemical field requires grid-based discretization [Fig. 11(a)], the immersed boundary method (IBM) is employed to approximate the point source (located at the center of the droplet). In the simulation, we replace the Dirac delta function $\delta(\boldsymbol{r}_p)$ with a regularized kernel function on grids,[94]

$$\delta(\boldsymbol{r}_p) \approx \sum_k \delta_h(\boldsymbol{r}_k - \boldsymbol{r}_p), \tag{D1}$$

where k runs over all grid points, and δ_h is the regularized delta function defined as

$$\delta_h = \prod_{\mu=1}^{d} \frac{1}{h}\varphi\left(\frac{\Delta r_\mu}{h}\right), \tag{D2}$$

where h is the lattice spacing, d is the dimension, and Δr_μ is the μ component of the distance between the grid point $\boldsymbol{r}_k$ and the point $\boldsymbol{r}_p$ of the delta function located. The distribution kernel, $\varphi(r)$, specifies the shape of the regularized delta function,[95]

$$\varphi(r) = \begin{cases} 1 - \frac{1}{2}|r| - |r|^2 + \frac{1}{2}|r|^3, & 0 \leqslant |r| < 1, \\ 1 - \frac{11}{6}|r| + |r|^2 - \frac{1}{6}|r|^3, & 1 \leqslant |r| < 2, \\ 0, & 2 \leqslant |r|. \end{cases} \tag{D3}$$

Figures 11(b) and 11(c) demonstrate a quantitative agreement between our numerical method and the theoretical result [Eq. (E1)] for the concentration.

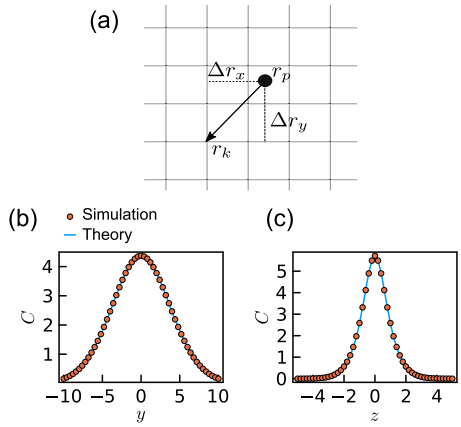

FIG. 11. Computation of the concentration field. (a) The schematic of the IBM method in the 2D gird. (b) and (c) Comparison of the concentration between the IBM method and analytical solution in 2D (b) and 3D (d). We initially set the droplet to move straightly along the x axis from the origin at a constant velocity $v_0 = 1$. We then measure the concentration along the y axis (and z axis, in the case of 3D simulation) at the point where $x = 0$. These simulation results agree with the analytical solutions.

22 January 2025 20:28:18

Published under an exclusive license by AIP Publishing

APPENDIX E: MESH-FREE METHOD

The concentration and the corresponding chemical gradient can be calculated via Green's function approach, alternatively. Assuming a point source with emission rate $Q_0 = 1$ moving in a trajectory $\boldsymbol{r}'(t')$, and released at all times $0 < t' < t$, the solution of Eq. (4) is Green's function convoluted over the particle trajectory $\boldsymbol{r}'$,[73,90]

$$C(\boldsymbol{r},t) = \int_0^t \left(\frac{\mathrm{Pe}}{4\pi(t-t')}\right)^{d/2} \exp\left(-\frac{|\boldsymbol{r}-\boldsymbol{r}'|^2\mathrm{Pe}}{4(t-t')}\right)\mathrm{d}t', \tag{E1}$$

where d is the dimension of the system, and the gradient field can be directly calculated as

$$\nabla|_r C(\boldsymbol{r},t) = -2\int_0^t \frac{\boldsymbol{r}-\boldsymbol{r}'}{\pi^{d/2}}\left(\frac{\mathrm{Pe}}{4(t-t')}\right)^{d/2+1} \exp\left(-\frac{|\boldsymbol{r}-\boldsymbol{r}'|^2 Pe}{4(t-t')}\right)\mathrm{d}t'. \tag{E2}$$

Similar to the finite difference method, in order to obtain the chemotactic force using Eq. (5), we need to calculate the mean of the surface gradient. In this method, we can directly obtain the gradient at the surface through integration using Eq. (E2). This approach allows us to avoid discretizing the space into grids and provides a more accurate result. However, since it directly calculates the gradients at specific points, it lacks comprehensive information on the full concentration field.

APPENDIX F: ANALYSIS OF THE CHEMICAL FIELD GRADIENT

The chemical field gradient $\nabla|_r C(\boldsymbol{r},t)$ is highly related to the velocity profile of Pe [Eq. (5)]. When Pe is small, the exponential term in Eq. (E2) approaches to 1; hence, $\nabla|_r$ is depending on the on the first term, i.e., $\nabla|_r \propto \left(\frac{\mathrm{Pe}}{4(t-t')}\right)^{d/2+1}$.

In the exponential term, we can choose $(t-t')$ equal to the period of the chiral trajectory T, then $\boldsymbol{r}-\boldsymbol{r}'$ is the corresponding pitch p. This implies that the term $\exp\left(-\frac{p^2 Pe}{4T}\right)$ captures the effect of the historical path. When Pe is small, the historical path continues to have a significant impact on the droplet. However, as Pe becomes larger ($\mathrm{Pe} \gg 4T/p^2$), only the historical path within a pitch significantly contributes to the auto-chemotactic force. Therefore, $\nabla|_r$ slowly decays.

APPENDIX G: CROSS SECTION

The emergence of the curling trajectory in 2D is due to the symmetry breaking in the concentration field. Our measurements of the concentration field distribution across the diameter (d) of the curling trajectory reveal a bias toward the right-hand side (negative skewness $\tilde{\mu}_3 = \frac{\sum_i^N (C_i-\bar{C})^3}{(N-1)\sigma^3}$), resulting in a counterclockwise trajectory with a handedness preference consistent with our institution. Meanwhile, we have not observed similar emergent curvature in 3D due to the absence of a comparable bias in the chemical trail.

APPENDIX H: ANALYSIS

We utilize the auto-correlation function (ACF) of the droplet velocity v_1 to gain a quantitative understanding of the trajectory's geometry and emergent behavior,

$$\mathrm{ACF}(\Delta t) = \frac{\langle \mathbf{v}_1(t)\cdot\mathbf{v}_1(t+\Delta t)\rangle}{\langle \mathbf{v}_1(t)\rangle^2}, \tag{H1}$$

where Δt represents the time lag and $\langle\cdots\rangle$ denotes the time average. We can extract the temporal correlations in the droplet's orientation by analyzing the ACF. We then apply the FFT method to the ACF to obtain the angular velocity ω_1 and the period of orientation $T = 2\pi/\omega_1$. We calculated the moving average position over five periods to obtain the emergent trajectory $\langle\tilde{\boldsymbol{r}}(t)\rangle$. The mean velocity $\langle\mathbf{v}_1\rangle$ is calculated from the trajectories using the formula $\langle\mathbf{v}_1\rangle = \langle\boldsymbol{r_p}(t+\Delta t) - \boldsymbol{r_p}(t)\rangle$, while the mean emergent velocity is obtained from the emergent trajectory using the formula $\langle\mathbf{v}_2\rangle = \langle\tilde{\boldsymbol{r}}(t+5T) - \tilde{\boldsymbol{r}}(t)\rangle$. The pitch of the emerging curling trajectory in 2D and the helical trajectory in 3D is measured by $p = \langle v_2\rangle T$.

REFERENCES

[1] A. Zöttl and H. Stark, J. Phys.: Condens. Matter **28**, 253001 (2016).
[2] M. C. Marchetti, J.-F. Joanny, S. Ramaswamy, T. B. Liverpool, J. Prost, M. Rao, and R. A. Simha, Rev. Mod. Phys. **85**, 1143 (2013).
[3] C. Reichhardt, A. Libál, and C. Reichhardt, Europhys. Lett. **139**, 27001 (2022).
[4] S. Tanaka, D. Sichau, and D. Iber, Bioinformatics **31**, 2340 (2015).
[5] Y. Wu, A. Fu, and G. Yossifon, Sci. Adv. **6**, eaay4412 (2020).
[6] K. Beppu, Z. Izri, J. Gohya, K. Eto, M. Ichikawa, and Y. T. Maeda, Soft Matter **13**, 5038 (2017).
[7] T. Bhattacharjee and S. S. Datta, Nat. Commun. **10**, 2075 (2019).
[8] H. Xu, J. Dauparas, D. Das, E. Lauga, and Y. Wu, Nat. Commun. **10**, 1792 (2019).
[9] A. C. Tsang, E. Demir, Y. Ding, and O. S. Pak, Adv. Intell. Syst. **2**, 1900137 (2020).
[10] T. Vicsek, A. Czirók, E. Ben-Jacob, I. Cohen, and O. Shochet, Phys. Rev. Lett. **75**, 1226 (1995).
[11] J. Toner and Y. Tu, Phys. Rev. Lett. **75**, 4326 (1995).
[12] F. Schmidt, B. Liebchen, H. Löwen, and G. Volpe, J. Chem. Phys. **150**, 094905 (2019).
[13] J. Bickmann and R. Wittkowski, Phys. Rev. Res. **2**, 033241 (2020).
[14] T. Sanchez, D. T. N. Chen, S. J. DeCamp, M. Heymann, and Z. Dogic, Nature **491**, 431 (2012).
[15] R. Zhang, A. Mozaffari, and J. J. de Pablo, Nat. Rev. Mater. **6**, 437 (2021).
[16] J. J. Keya, R. Suzuki, A. M. R. Kabir, D. Inoue, H. Asanuma, K. Sada, H. Hess, A. Kuzuya, and A. Kakugo, Nat. Commun. **9**, 453 (2018).
[17] A. C. Tsang, A. T. Lam, and I. H. Riedel-Kruse, Nat. Phys. **14**, 1230 (2018).
[18] S. Yang, M. Huang, Y. Zhao, and H. Zhang, Phys. Rev. Lett. **126**, 058001 (2021).
[19] B. M. Friedrich and F. Jülicher, Proc. Natl. Acad. Sci. U. S. A. **104**, 13256 (2007).
[20] J. Palacci, S. Sacanna, A. P. Steinberg, D. J. Pine, and P. M. Chaikin, Science **339**, 936 (2013).
[21] X. Fu, S. Kato, J. Long, H. H. Mattingly, C. He, D. C. Vural, S. W. Zucker, and T. Emonet, Nat. Commun. **9**, 2177 (2018).
[22] N. Mittal, E. O. Budrene, M. P. Brenner, and A. Van Oudenaarden, Proc. Natl. Acad. Sci. U. S. A. **100**, 13259 (2003).
[23] J. Adler, Science **153**, 708 (1966).
[24] W. T. Kranz, A. Gelimson, K. Zhao, G. C. L. Wong, and R. Golestanian, Phys. Rev. Lett. **117**, 038101 (2016).
[25] A. V. Narla, D. B. Borenstein, and N. S. Wingreen, Proc. Natl. Acad. Sci. U. S. A. **118**, e2022818118 (2021).
[26] W. J. Ridgway, M. P. Dalwadi, P. Pearce, and S. J. Chapman, Phys. Rev. Lett. **131**, 228302 (2023).

22 January 2025 20:28:18

Published under an exclusive license by AIP Publishing

[27]A. Fischer, F. Schmid, and T. Speck, Phys. Rev. E **101**, 012601 (2020).
[28]M. P. Dalwadi and P. Pearce, Proc. Natl. Acad. Sci. U. S. A. **118**, e2022312118 (2021).
[29]S. J. Ebbens and J. R. Howse, Soft Matter **6**, 726 (2010).
[30]R. Kailasham and A. S. Khair, Phys. Rev. E **107**, 044609 (2023).
[31]O. Dauchot and H. Löwen, J. Chem. Phys. **151**, 114901 (2019).
[32]F. Lancia, T. Yamamoto, A. Ryabchun, T. Yamaguchi, M. Sano, and N. Katsonis, Nat. Commun. **10**, 5238 (2019).
[33]B. Nakayama, H. Nagase, H. Takahashi, Y. Saito, S. Hatayama, K. Makino, E. Yamamoto, and T. Saiki, Proc. Natl. Acad. Sci. U. S. A. **120**, e2213713120 (2023).
[34]A. Walther and A. H. Müller, Soft Matter **4**, 663 (2008).
[35]H. R. Vutukuri, M. Lisicki, E. Lauga, and J. Vermant, Nat. Commun. **11**, 2628 (2020).
[36]J. Katuri, R. Poehnl, A. Sokolov, W. Uspal, and A. Snezhko, Sci. Adv. **8**, eabo3604 (2022).
[37]B. D. Frank, S. Djalali, A. W. Baryzewska, P. Giusto, P. H. Seeberger, and L. Zeininger, Nat. Commun. **13**, 2562 (2022).
[38]A. Nourhani, S. J. Ebbens, J. G. Gibbs, and P. E. Lammert, Phys. Rev. E **94**, 030601 (2016).
[39]A. Kirvin, D. Gregory, A. Parnell, A. I. Campbell, and S. Ebbens, Mater. Adv. **2**, 7045 (2021).
[40]R. J. Archer, A. I. Campbell, and S. J. Ebbens, Soft Matter **11**, 6872 (2015).
[41]B. V. Hokmabad, A. Nishide, P. Ramesh, C. Krüger, and C. C. Maass, Soft Matter **18**, 2731 (2022).
[42]A. Ziepke, I. Maryshev, I. S. Aranson, and E. Frey, Nat. Commun. **13**, 6727 (2022).
[43]B. V. Hokmabad, K. A. Baldwin, C. Krüger, C. Bahr, and C. C. Maass, Phys. Rev. Lett. **123**, 178003 (2019).
[44]J. Zheng, J. Chen, Y. Jin, Y. Wen, Y. Mu, C. Wu, Y. Wang, P. Tong, Z. Li, X. Hou, and J. Tang, Nature **617**, 499 (2023).
[45]J. Van Der Kolk, F. Raßhofer, R. Swiderski, A. Haldar, A. Basu, and E. Frey, Phys. Rev. Lett. **131**, 088201 (2023).
[46]B. V. Hokmabad, J. Agudo-Canalejo, S. Saha, R. Golestanian, and C. C. Maass, Proc. Natl. Acad. Sci. U. S. A. **119**, e2122269119 (2022).
[47]H. Zhao, A. Košmrlj, and S. S. Datta, Phys. Rev. Lett. **131**, 118301 (2023).
[48]E. Lushi, R. E. Goldstein, and M. J. Shelley, Phys. Rev. E **98**, 052411 (2018).
[49]S. Ebbens, R. A. L. Jones, A. J. Ryan, R. Golestanian, and J. R. Howse, Phys. Rev. E **82**, 015304 (2010).
[50]R. Seemann, J.-B. Fleury, and C. C. Maass, Eur. Phys. J.: Spec. Top. **225**, 2227 (2016).
[51]J. R. Howse, R. A. Jones, A. J. Ryan, T. Gough, R. Vafabakhsh, and R. Golestanian, Phys. Rev. Lett. **99**, 048102 (2007).
[52]X. Wang, R. Zhang, A. Mozaffari, J. J. de Pablo, and N. L. Abbott, Soft Matter **17**, 2985 (2021).
[53]S. Suda, T. Suda, T. Ohmura, and M. Ichikawa, Phys. Rev. E **106**, 034610 (2022).
[54]T. Yamamoto and M. Sano, Soft Matter **13**, 3328 (2017).
[55]T. Yamamoto and M. Sano, Phys. Rev. E **97**, 012607 (2018).
[56]S. Herminghaus, C. C. Maass, C. Krüger, S. Thutupalli, L. Goehring, and C. Bahr, Soft Matter **10**, 7008 (2014).
[57]C. Krüger, G. Klös, C. Bahr, and C. C. Maass, Phys. Rev. Lett. **117**, 048003 (2016).
[58]C. Jin, J. Vachier, S. Bandyopadhyay, T. Macharashvili, and C. C. Maass, Phys. Rev. E **100**, 040601 (2019).
[59]J. F. Jikeli, L. Alvarez, B. M. Friedrich, L. G. Wilson, R. Pascal, R. Colin, M. Pichlo, A. Rennhack, C. Brenker, and U. B. Kaupp, Nat. Commun. **6**, 7985 (2015).
[60]E. Lauga, W. R. DiLuzio, G. M. Whitesides, and H. A. Stone, Biophys. J. **90**, 400 (2006).
[61]A. Negi, K. Beppu, and Y. T. Maeda, Phys. Rev. Res. **5**, 023196 (2023).
[62]C. W. Chan, D. Wu, K. Qiao, K. L. Fong, Z. Yang, Y. Han, and R. Zhang, Nat. Commun. **15**, 1406 (2024).
[63]M. Akter, J. J. Keya, K. Kayano, A. M. R. Kabir, D. Inoue, H. Hess, K. Sada, A. Kuzuya, H. Asanuma, and A. Kakugo, Sci. Robot. **7**, eabm0677 (2022).
[64]N. C. X. Stuhlmüller, F. Farrokhzad, P. Kuświk, F. Stobiecki, M. Urbaniak, S. Akhundzada, A. Ehresmann, T. M. Fischer, and D. De Las Heras, Nat. Commun. **14**, 7517 (2023).
[65]P. Dwivedi, D. Pillai, and R. Mangal, Curr. Opin. Colloid Interface Sci. **61**, 101614 (2022).
[66]A. Zöttl and H. Stark, Annu. Rev. Condens. Matter Phys. **14**, 109 (2023).
[67]D. Sondak, C. Hawley, S. Heng, R. Vinsonhaler, E. Lauga, and J.-L. Thiffeault, Phys. Rev. E **94**, 062606 (2016).
[68]W.-F. Hu, T.-S. Lin, S. Rafai, and C. Misbah, Phys. Rev. Lett. **123**, 238004 (2019).
[69]M. Morozov and S. Michelin, J. Chem. Phys. **150**, 044110 (2019).
[70]S. Michelin, E. Lauga, and D. Bartolo, Phys. Fluids **25**, 061701 (2013).
[71]T. Yamamoto and M. Sano, Phys. Rev. E **99**, 022704 (2019).
[72]S. Saha, S. Ramaswamy, and R. Golestanian, New J. Phys. **21**, 063006 (2019).
[73]J. Taktikos, V. Zaburdaev, and H. Stark, Phys. Rev. E **84**, 041924 (2011).
[74]C. Jin, C. Krüger, and C. C. Maass, Proc. Natl. Acad. Sci. U. S. A. **114**, 5089 (2017).
[75]F. J. Sevilla, Phys. Rev. E **94**, 062120 (2016).
[76]F. Kümmel, B. Ten Hagen, R. Wittkowski, I. Buttinoni, R. Eichhorn, G. Volpe, H. Löwen, and C. Bechinger, Phys. Rev. Lett. **110**, 198302 (2013).
[77]G. Li and D. L. Koch, J. Fluid Mech. **952**, A16 (2022).
[78]A. Nourhani, P. E. Lammert, A. Borhan, and V. H. Crespi, Phys. Rev. E **87**, 050301 (2013).
[79]F. Siebers, A. Jayaram, P. Blümler, and T. Speck, Sci. Adv. **9**, eadf5443 (2023).
[80]J. S. Dai, Mech. Mach. Theory **92**, 144 (2015).
[81]B. V. Hokmabad, R. Dey, M. Jalaal, D. Mohanty, M. Almukambetova, K. A. Baldwin, D. Lohse, and C. C. Maass, Phys. Rev. X **11**, 011043 (2021).
[82]J. G. Lee, A. M. Brooks, W. A. Shelton, K. J. M. Bishop, and B. Bharti, Nat. Commun. **10**, 2575 (2019).
[83]Z. Izri, M. N. Van Der Linden, S. Michelin, and O. Dauchot, Phys. Rev. Lett. **113**, 248302 (2014).
[84]S. Michelin, Annu. Rev. Fluid Mech. **55**, 77 (2023).
[85]R. Zhang and J. Koplik, Phys. Rev. E **85**, 026314 (2012).
[86]Y. Takaha and D. Nishiguchi, Phys. Rev. E **107**, 014602 (2023).
[87]S. Suda, T. Suda, T. Ohmura, and M. Ichikawa, Phys. Rev. Lett. **127**, 088005 (2021).
[88]A. Kulkarni, E. Vidal-Henriquez, and D. Zwicker, Sci. Rep. **13**, 733 (2023).
[89]R. Maity and P. S. Burada, Phys. Fluids **35**, 043611 (2023).
[90]S. Saha, R. Golestanian, and S. Ramaswamy, Phys. Rev. E **89**, 062316 (2014).
[91]J. Stürmer, M. Seyrich, and H. Stark, J. Chem. Phys. **150**, 214901 (2019).
[92]M. Suga, S. Suda, M. Ichikawa, and Y. Kimura, Phys. Rev. E **97**, 062703 (2018).
[93]M. X. Fernandes and J. G. de la Torre, Biophys. J. **83**, 3039 (2002).
[94]Y. Bao, A. D. Kaiser, J. Kaye, and C. S. Peskin, J. Comput. Phys. **316**, 139 (2016); arXiv:1505.07529 [physics].
[95]A.-K. Tornberg and B. Engquist, J. Comput. Phys. **200**, 462 (2004).

22 January 2025 20:28:18

Published under an exclusive license by AIP Publishing